Nuclear Science and Techniques (2026) 37:116
https://doi.org/10.1007/s41365-026-01923-4

Development of an antenna adjustable fundamental power coupler for the 81.25 MHz superconducting cavity at the High Intensity Heavy-Ion Accelerator Facility

Guo-Chang Liu[1,2] · Tian-Cai Jiang[1] · Zong-Heng Xue[1] · Ji-Yu Wang[1] · Ke-An Jin[1] · Meng-Xin Xu[1] · Zhou-Li Zhang[1] · Chun-Long Li[1] · Qi-Tong Huang[3] · Sheng-Xue Zhang[1] · Sheng-Hu Zhang[1] · Yuan He[1]

Received: 24 August 2024 / Revised: 26 December 2024 / Accepted: 1 January 2025 / Published online: 10 April 2026

Abstract
The Institute of Modern Physics (IMP) of the Chinese Academy of Sciences (CAS) has designed and prototyped fundamental power couplers for 81.25 MHz superconducting quarter-wave resonators (QWR) in the High-Intensity Heavy-Ion Accelerator Facility (HIAF). The QWR coupler operates in the pulsed or continuous-wave mode with an average power of 6 kW. This coupler is designed with a 50 Ω coaxial structure and a dual-disk warm-window assembly. Focusing on the optimized heat leakage, a double-walled structure is applied to the outer conductor of the coupler for helium gas cooling at 5 K. To suppress multipacting (MP), a 10-nm titanium nitride (TiN) coating is applied to the vacuum side of the ceramic window, whereas a DC bias voltage is applied to the inner conductor. To reduce the production cost of the coupler and make it suitable for mass production, various coupler fabrication materials were tested, and the feasibility of the fabrication process was verified. The coupler includes two types of diagnostic ports for vacuum and ARC monitoring. Two prototype couplers were fabricated and tested for high-power conditioning. The QWR couplers proved their robustness with 10 h of 9 kW traveling-wave conditioning and 12 h of 9 kW standing wave conditioning, achieving a stabilized 9 kW power level and a stable vacuum. As predicted, MP barriers were encountered at input powers ranging from 1 kW to 9 kW, and a DC bias voltage of 800 V effectively suppressed the occurrence of MP.

Keywords 81.25 MHz fundamental power coupler · Superconducting quarter-wave resonator · High-power conditioning

1 Introduction

The High-Intensity Heavy-Ion Accelerator Facility (HIAF) proposed by the Institute of Modern Physics (IMP) of the Chinese Academy of Sciences (CAS) is a next-generation platform for the exploration of exotic nuclear structures [1], precise mass measurements of atomic nuclei [2–5], and fusion physics [6]. The facility integrates several key components, including a superconducting electron cyclotron resonance (SECR) ion source, a superconducting ion linear accelerator (iLinac), a booster synchrotron (BRing), and a high-precision spectrometer ring (SRing) [7]. In iLinac, a superconducting quarter-wave resonator (QWR) is one of the main acceleration structures, optimized for a relative velocity of 0.07 and an operating frequency of 81.25 MHz, which facilitates the acceleration of low-energy ions and protons [8]. The iLinac utilizes six QWR cryomodules for beam acceleration, each comprising five QWRs for a total of 30 QWRs. These QWRs are critical for boosting the energy of $^{238}U^{35+}$ ions with a beam current of 1 emA from 0.8 MeV/u to 5.3 MeV/u, which requires strong coupling. Using Eq. (1) and (2) [9], the required RF operating power of the QWR superconducting cavity at the designed beam

This work was supported by the Large Research Infrastructures "High-Intensity Heavy-Ion Accelerator Facility" (No. 2017-000052-73-01-002107).

✉ Tian-Cai Jiang
jiangtiancai@impcas.ac.cn

1 Institute of Modern Physics, Chinese Academy of Sciences, Lanzhou 730000, China

2 University of Chinese Academy of Sciences, Beijing 100049, China

3 Advanced Energy Science and technology Guangdong Laboratory, Huizhou 516001, China

intensity can be calculated. These equations contain many parameters of the superconducting cavity, such as its $\frac{R}{Q}$, fundamental mode resonance frequency f_0, and accelerating voltage V_{acc}. The detuning frequency Δf indicates the difference between the resonant and practical frequencies caused by helium pressure fluctuations, Lorentz detuning, and mechanical noise (microphonics). The parameters I_{beam} and ϕ_{b} of the iLinac represent its average beam intensity and synchronous phase, respectively. These parameters are listed in Table 1, where the synchronous phase is selected as −45°. The detuning frequency is −90 Hz, with the mechanical noise detuning contributing −50 Hz [10]. Therefore, an average power of 6 kW is required per QWR at the designed beam intensity.

The fundamental power coupler (FPC) is a critical and sensitive component of superconducting cavity systems. Its task is to transfer RF power to the superconducting cavity while maintaining a vacuum between the power source and the superconducting cavity. The FPC is also a thermal bridge between ambient (300 K) and cryogenic (2 K) temperatures, which significantly increases the complexity of its design [11]. Several key factors must be considered in designing an FPC system. First, the coupler requires a wide bandwidth to ensure optimal transmission performance. Second, an effective cooling design is crucial for minimizing total heat leakage and reducing heat transfer to the superconducting cavity system [12]. Third, the multipacting (MP) effect within the coupler can lead to ceramic window breakage. Therefore, effective suppression methods must be implemented [13]. Finally, the coupler must have high mechanical strength to withstand harsh conditions during its transportation, installation, and operation. In addition to these design considerations, the development of FPCs for superconducting cavities must focus on selecting viable and repeatable mechanical designs and manufacturing processes to facilitate mass production and reduce production time [14]. In addition, establishing a stable and efficient high-power conditioning procedure is critical for minimizing the conditioning time required for couplers [15].

Table 1 Main parameters of the FPC, QWR, and iLinac

Parameters	Specification
Parameters related to coupler	
Frequency (MHz)	81.25
Operating power (kW)	6 (CW)
Adjusting length (mm)	±10
Q_{e}	$1.8 \times 10^5 \sim 4.1 \times 10^5$
Half bandwidth (S11< −20 dB) (MHz)	> 2
FPC type	Coaxial capacitive type
Window type	Dual (warm)
Ceramic window material and type	96.7% alumina & disk
Coupling type	Electrical coupling
Impedance (Ω)	50
Cooling method	5 K gas helium
Coupling adjusting	Yes
Parameters related to QWR	
Effective length L_{eff} (m)	0.258
$E_{\mathrm{peak}}/E_{\mathrm{acc}}$	4.69
E_{acc} (MV/m)	5.97
V_{acc} (MV)	1.54
R/Q (Ω)	485.70
Q_0	1.43×10^9
$\mathrm{d}f/\mathrm{d}p$ (Hz/mbar)	−2.52
LFD (Hz/(MV/m)^2)	−1.28
Parameters related to iLinac	
Average beam intensity I_{beam} (emA)	1
Operating mode	CW/ pulse
Synchronous phase ϕ_{b} (degree)	$-45 \sim -26$

$$Q_{\mathrm{ext}} = \left[\left(\frac{R}{Q}\frac{I_{\mathrm{beam}}}{V_{\mathrm{acc}}}\right)^2 + \left(\frac{2\Delta f}{f_0}\right)^2 + 2\left(\frac{R}{Q}\frac{I_{\mathrm{beam}}}{V_{\mathrm{acc}}}\right)\left(\frac{2\Delta f}{f_0}\right)\sin\phi_{\mathrm{b}}\right]^{-\frac{1}{2}} \quad (1)$$

$$P = \frac{V_{\mathrm{acc}}^2}{4\frac{R}{Q}Q_{\mathrm{ext}}}\left[\left(1 + \frac{R}{Q}Q_{\mathrm{ext}}\frac{I_{\mathrm{beam}}}{V_{\mathrm{acc}}}\cos\phi_{\mathrm{b}}\right)^2 + \left(2Q_{\mathrm{ext}}\frac{\Delta f}{f_0} + \frac{R}{Q}Q_{\mathrm{ext}}\frac{I_{\mathrm{beam}}}{V_{\mathrm{acc}}}\sin\phi_{\mathrm{b}}\right)^2\right] \quad (2)$$

In accelerators, most couplers are based on coaxial transmission lines. The HIAF QWR coupler was chosen to utilize coaxial FPCs owing to its compact geometry, simple MP suppression, and lower heat leakage. To balance complexity and reliability, many couplers utilize a single-window design to satisfy specific design requirements. The 166.6 MHz FPC designed for the HEPS project utilizes a single warm window with a choke structure to ensure impedance matching and a lower electric field at the brazed joints. This is highly suitable for high-power couplers because it effectively protects the vacuum system of the superconducting cavity [16]. The ceramic window schemes for QWR couplers used in the RISP [17] and SPIRAL2 [18] projects are similar in that the ceramic window utilizes a tapered structure to connect to the coaxial section to ensure good transmission characteristics. This ceramic window assembly is easy to machine and suitable for couplers at medium power levels. QWR couplers employed in the NICA [19], FIRB [20], ATLAS [21], and RIKEN [22] projects utilize a cold/warm dual-window design that provides protection against superconducting cavity contamination. The NICA coupler uses a transition structure from the pillbox design of the fixed ceramic window to the coaxial section of the coupler to achieve good transmission performance. The FIRB, ATLAS, and RIKEN couplers facilitate good transmission by adjusting the distance and dimensions of the two ceramic windows. Compared with cylindrical ceramic windows, disk-shaped windows are easier to fabricate and are not limited by peak voltages [23]. The ceramic window of the coupler for the 25 MeV superconducting linear accelerator demonstration facility of the China Initiative Accelerator Driven System (CiADS) project broke repeatedly because of the emission of electrons from the superconducting cavity. To avoid this problem, a dual-disk warm-ceramic-window assembly was used in our QWR coupler to further reduce the risk of vacuum leakage in the superconducting cavity system.

Figure 1 shows a detailed schematic of the structure of the HIAF 81.25 MHz FPC, which consists of four subassemblies: a coupling antenna, a coupler transmission section, a dual-disk warm-window assembly, and a T-transition structure (T-box). The dual-disk warm-window assembly is part of the vacuum assembly and separates the vacuum from air. The antenna adjustment method for the QWR coupler uses bellows on the vacuum side of the outer conductor of the coupler [21], and the depth of penetration of the antenna can be adjusted by stretching or compressing the bellows and varies within ± 10 mm. Table 2 summarizes the status of research on QWR couplers conducted by various research institutes [17, 19–22]. To adjust the insertion depth of the antenna, NICA, FRIB, ATLAS, and RIKEN adopted a solution similar to ours of incorporating bellows into the outer conductor of the vacuum section of the coupler. In the cooling scheme design, the QWR couplers used by RISP, FRIB, ATLAS, and RIKEN incorporate a thermal interceptor design to minimize total heat leakage. However, the NICA project utilizes a liquid helium and liquid nitrogen immersion scheme for this purpose. The design parameters of the HIAF QWR coupler are listed in Table 1, HIAF QWR couplers utilize helium gas at 5 K to cool the outer conductor of the coupler and reduce heat leakage.

This study focuses on the development of QWR couplers. The QWR coupler designed by our team has successfully completed a high-power conditioning test and meets the long-term stable operation requirements of HIAF. The

Table 2 Design parameters of QWR fundamental power couplers used in various research institutes

Parameters	NICA	RISP	FRIB	ATLAS	RIKEN
Frequency (MHz)	162	81.25	80.5	72.75	75.5
Operating power (kW)	30	2	4	4	10
Impedance (Ω)	50	50	50	50	50
Window type	Dual (cold+warm)	Single (warm)	Dual (cold+warm)	Dual (cold+warm)	Dual (cold+warm)
Ceramic window shape	Disk	Disk	Disk	Disk	Disk
Ceramic window material	95% alumina	99.9% alumina	97.6% alumina	96% alumina	99.5% alumina
Coupling adjusting	Yes	No	Yes	Yes	Yes
Cooling method	Liquid helium and nitrogen	40 K thermal anchor	55 K thermal anchor	80 K thermal anchor	40 K thermal anchor

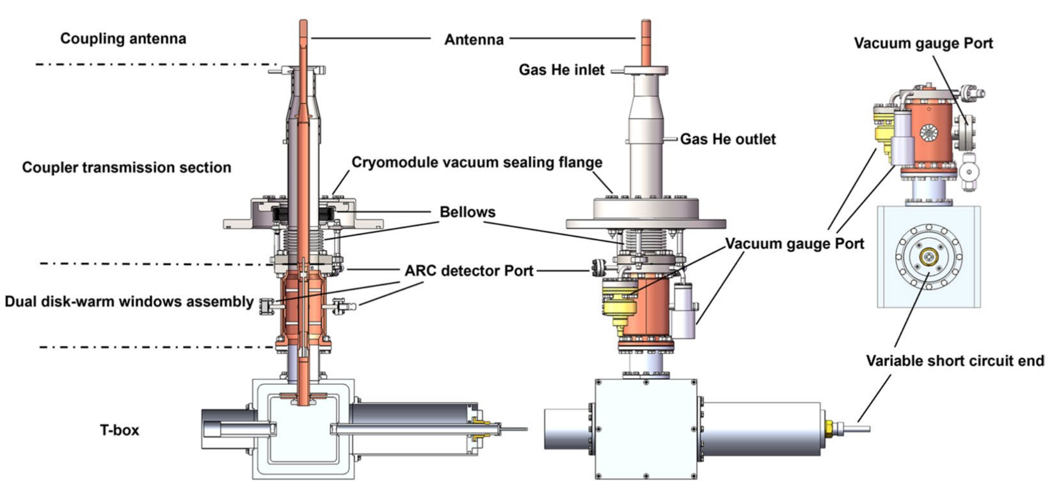

Fig. 1 (Color online) Schematic of the mechanical structure of the HIAF QWR fundamental power coupler

remainder of this paper is organized as follows. Section 2 describes the RF design of our QWR coupler. Section 3 describes the thermal analysis and cooling design of the QWR coupler. Section 4 discusses its MP effect and the methods to suppress this effect. Section 5 describes the mechanical design, analysis, and machining of QWR couplers. Section 6 discusses the high-power conditioning test for QWR couplers and MP validation. Finally, the study's conclusions are presented in Sect. 7.

2 Fundamental power coupler RF design

The RF design of the FPC is intended to maximize the power transfer to the beam-loaded superconducting cavity, minimize the risk of ceramic window rupture due to ARC or MP, and provide a significant margin of safety. The RF design of the QWR coupler is divided into the design of four parts: the T-box, dual-disk warm-window assembly, coupler transmission section, coupling antenna design of the coupler, and coupling to the superconducting cavity. Figure 2 shows the RF simulation model of the coupler and the related design parameters. The RF designs of the coupler were created using CST Microwave Studio [24].

The dimensions of the T-box include the outer box width LTboxouter, inner box width LTboxinner, outer conductor radius at the short circuit Lsc-outer, and short circuit length Lshort, as shown in Fig. 2. The T-box feeder end can be connected to a rigid coaxial line with an outer diameter of 79.4 mm and an inner diameter of 34 mm, and the coupling ports for the T-box connections have an inner radius of 13.04 mm and an outer radius of the interface of 30 mm. The inner conductor radius of the short circuit was determined to be 12 mm for production cost and compatibility with external monitoring devices. The final optimized parameter values are not unique because they are not independent of each other, and the final parameters must be determined in practical situations. The initial values of the parameters LTboxouter, LTboxinner, Lsc-outer, and Lshort were set as 160 mm, 100 mm, 20 mm, and 150 mm, respectively. LTboxouter and LTboxinner were first optimized for a suitable T-box volume and convenient installation using scanning steps of 5 mm and 10 mm, respectively. The values of these two parameters were initially determined to be 180 mm and 140 mm. Figure 3(a) shows the effect of varying the LTboxouter parameter on the transmission performance of the T-box at the initial values. Figure 3(b) shows the relationship between the transmission performance of the T-box and LTboxinner when LTboxouter is determined to be 180 mm. The parameters Lsc-outer and Lshort were optimized to ensure minimum reflection at the nominal frequency, as shown in Fig. 3(c) and (d). The final T-box dimension parameters, LTboxouter, LTboxinner, Lsc-outer, and Lshort, were 180 mm, 140 mm, 50 mm, and 230 mm, respectively. Figure 4(a) shows the optimized transmission performance of the T-box with when the S11 parameter is less than −70 dB at 81.25 MHz.

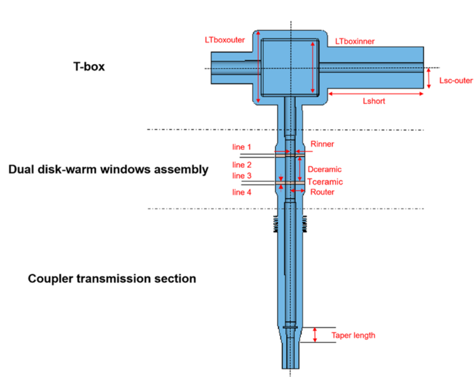

Fig. 2 (Color online) Simulation modeling of the coupler and related design parameters

The dual-disk warm-window assembly is a fragile and critical component of the FPC, and it utilizes a dual-disk window structure with a taper structure to ensure good transmission performance. Figure 2 shows the RF window model and related parameters. The dielectric constant of the ceramic window was determined to be 9.2 during the electromagnetic design process. The thickness of the ceramic window Tceramic directly affects the performance and production costs of the coupler. The height of the rectangular cryomodule and the difficulty of machining the component limit the distance Dceramic between the two ceramic windows, and the inner diameter Rinner and outer diameter Router of the ceramic windows are determined by the coaxial section of the connection. These parameters interact with each other and affect the transmission performance of the ceramic window assembly. A series of parameter sweeps was performed. First, we determined the thickness Tceramic of the ceramic window and the distance Dceramic between the two ceramic windows and then adjusted the inner diameter Rinner and outer diameter Router of the ceramic window. Finally, we searched for a suitable taper structure of the inner and outer conductors to achieve excellent transmission performance. Therefore, Tceramic, Dceramic, Rinner, and Router were selected to be 6 mm, 60 mm 11.5 mm, and 35 mm, respectively. The monitoring locations of the dual-disk warm-window assembly are shown in Fig. 2, with lines 1, 2, 3, and 4 located on the top and bottom surfaces of the first and second ceramic windows, respectively. The possibility of breakdown is determined by the distributed electric field on these lines. The electric field distributions on the top and bottom surfaces of the ceramic windows under an average traveling power of 6 kW are shown in Fig. 4(b).

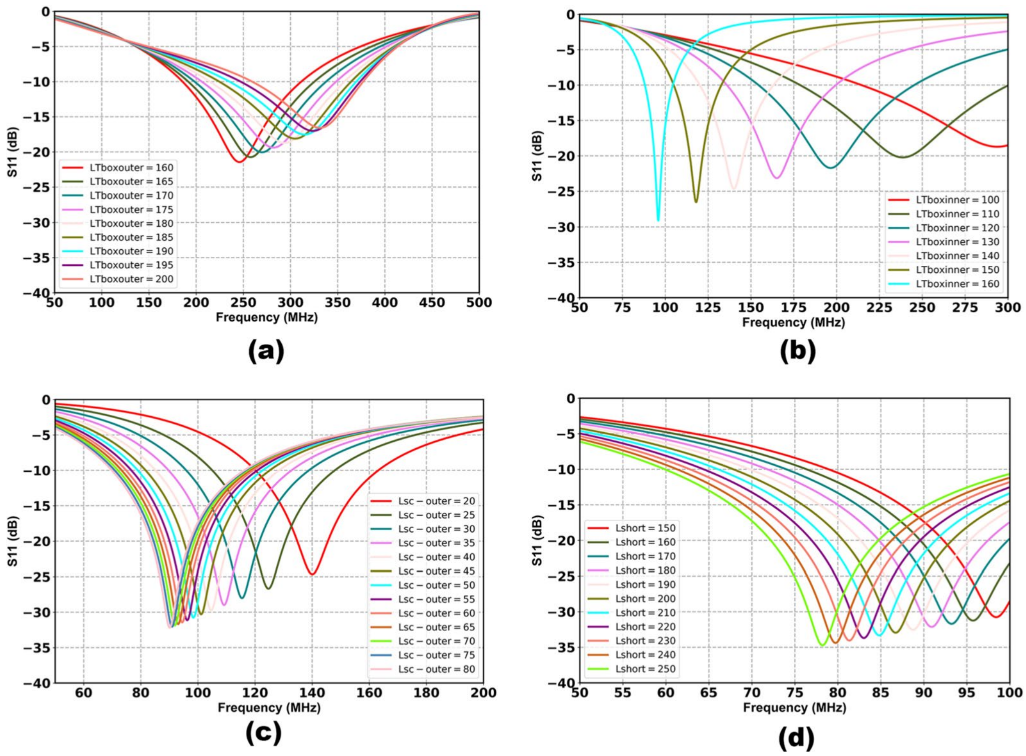

Fig. 3 (Color online) S11 parameters for T-box as functions of frequency. (**a**) Different widths of the outer box (LTboxouter). (**b**) Different widths of the inner box (LTboxinner). (**c**) Different radii of the outer conductor at the short-circuit end (Lsc-outer). (d) Different lengths of the short-circuit end (Lshort)

The maximum electric field in these regions was less than 0.065 MV/m, which is significantly lower than the breakdown electric field of 3 MV/m in ambient air [25].

The transmission section of the QWR coupler is based on a 50 Ω coaxial transmission line. To match the dimensions of the QWR superconducting cavity coupling port, it is necessary to smoothly change the radius of the outer conductor to that of the superconducting cavity coupling port. Figure 2 presents the design parameters of the transmission section of the coupler. The transmission performance varies with the taper length, as shown in Fig. 4(c). The return loss is minimized when the taper length is 65 mm. However, when the QWR superconducting cavity is in the no-beam state, the taper length depends on whether the ceramic window of the coupler is at a position where the electric field is relatively strong. The final choice of a taper length of 45 mm and an S11 parameter of −37 dB balanced the transmission performance and coupler length requirements. As shown in Fig. 5, the optimized position of the dual-disk warm-ceramic-window assembly was confirmed to be close to the standing wave node [26]. After optimizing the main FPC, the S11 value of the entire QWR coupler is as shown in Fig. 4(d). The return loss of the coupler was −72 dB at 81.25 MHz and less than −20 dB at a bandwidth of 14 MHz. To evaluate the effect of manufacturing errors in key design parameters of the coupler on the coupler performance, a manufacturing error of plus or minus 0.5 mm was assumed, which is much larger than the practical processing error. Figure 6 shows that the effect of the practical manufacturing error on the coupler performance is minimal, and the S11 parameter of the coupler for a manufacturing error of plus minus 0.5 mm in various design parameters of the coupler is still less than −25 dB at the operating frequency.

Electrical coupling facilitates power transmission between the coupler and QWR cavity. The coupler introduces RF power into the cavity through an antenna probe, which gradually generates an electromagnetic field inside the cavity. The ratio of the intrinsic quality factor Q_0 to the external quality factor Q_{ext} quantifies the coupling strength between the superconducting cavity and the FPC. The coupling strength is affected by the coupling port position, antenna diameter, antenna tip chamfer radius, and antenna insertion depth. The position of the coupling port is predetermined during the design of the superconducting cavity, while the antenna diameter is based on the characteristic impedance of 50 Ω. The external quality factor varies with the chamfer radius, as shown in Fig. 7(a). It is impractical to modify the chamfer radius during the actual operation of the coupler. Therefore, a chamfer radius of 3 mm was chosen. Figure 7(b) shows the variation in the external quality factor

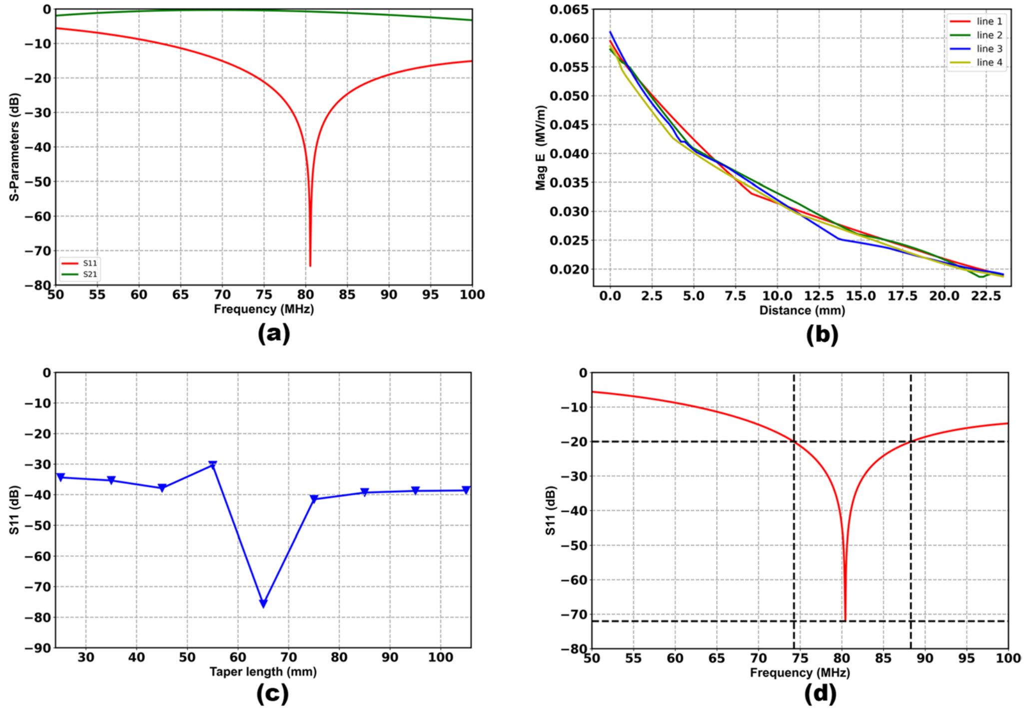

Fig. 4 (Color online) Relevant optimization results of QWR coupler subassemblies. (**a**) S11 and S21 parameters of the optimized T-box as functions of frequency. (**b**) Electric field distribution along the radial direction of the ceramic window after optimization. (**c**) Curves of the relationship between the taper length of the transmission part of the coupler and the S11 parameter at the operating frequency. (**d**) S11 parameter of the optimized QWR coupler as a function of frequency

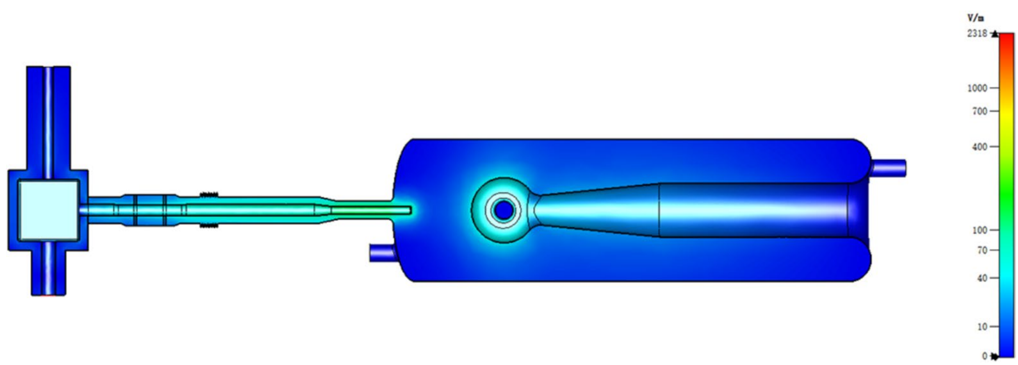

Fig. 5 (Color online) Standing wave electric field distribution in the QWR coupler and QWR superconducting cavity. The energy storage of the cavity is 1 J

Fig. 6 (Color online) Effect of manufacturing errors in critical parameters on coupler performance

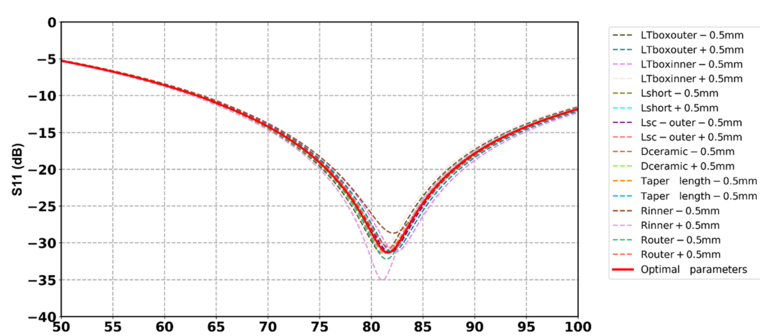

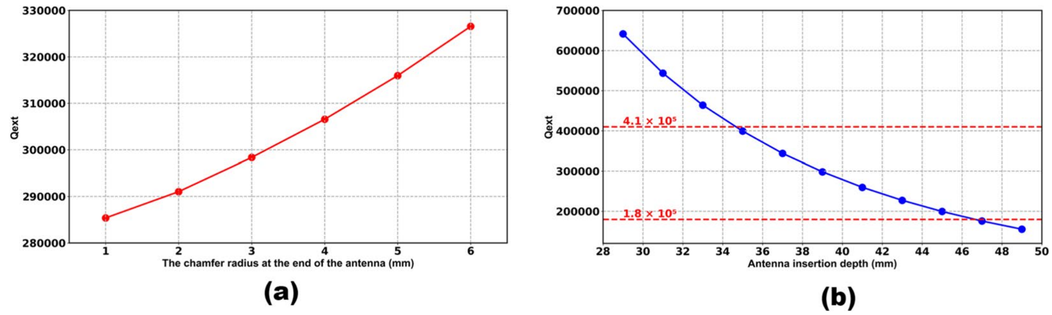

Fig. 7 (Color online) Variation of external quality factor with different parameters. (**a**) Variation of external quality factor with chamfer radius. (**b**) Variation of external quality factor with antenna insertion depth

with antenna insertion depth. The antenna insertion depth can be adjusted from 29 mm to 49 mm to obtain a wider range of external quality factor values than that specified in the coupler design requirements.

3 Thermal analysis and cooling design of the coupler

The FPC is the interface between the cryogenic and ambient environments and constitutes a significant thermal load in cryogenic systems. The thermal analysis and cooling design of the coupler aim to minimize the thermal load on the superconducting cavity through a simple design, while ensuring that the ceramic window does not rupture owing to thermal stress. To determine the temperature distribution of the coupler for the designed power operation and to design a suitable cooling method to ensure the stable operation of the superconducting cavity, thermal analysis simulations of the QWR coupler were performed using COMSOL [27].

The T-box connection flange and coupling port of the coupler were set to 300 K and 2 K, respectively. The material parameters used in the thermal analysis and cooling design are detailed in Ref. [28, 29]. Figure 8 shows the temperature distribution of the QWR coupler under various boundary conditions. Figure 8(a) shows the temperature distribution at the air end of the coupler's outer conductor with the heat transfer coefficient set to $0.1\ \mathrm{W/(m^2 \cdot K)}$, where the temperature near the cryomodule flange is less than the outside ambient temperature, and the water droplets are prone to condensation, which may accelerate oxidation of the material and damage the monitoring devices. Therefore, fans to cool the outer conductor were included on the air side of the coupler to prevent the condensation of water droplets; thus, a boundary condition with the forced convection heat transfer coefficient set to $5\ \mathrm{W/(m^2 \cdot K)}$ was applied to the outer conductor on the air side of the coupler. Figure 8(b) shows the temperature distribution of the coupler with forced convection heat transfer, where the temperature of the outer conductor at the air side of the coupler is close to 300 K, which prevents water droplets from condensing.

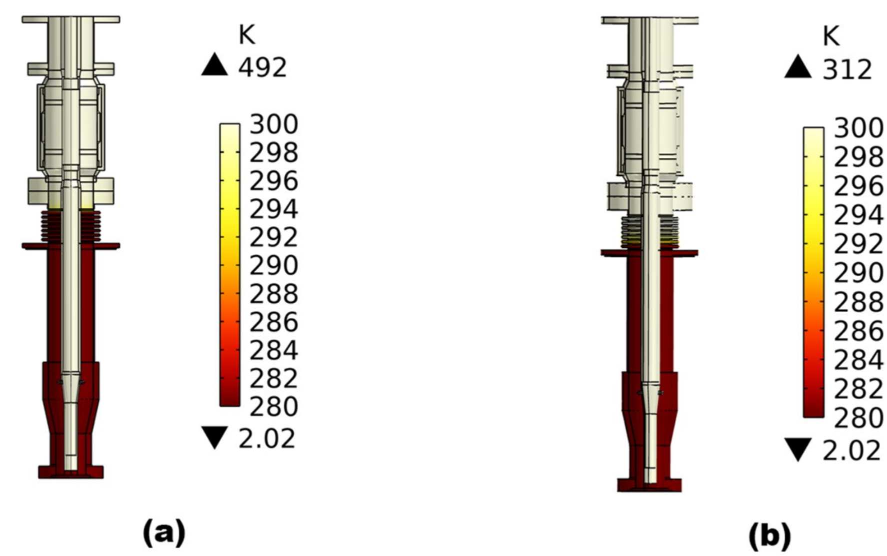

Fig. 8 (Color online) Temperature distribution of the QWR coupler. (**a**) The inner conductor of the coupler, and the outer conductor of the air side are set to a $0.1\ \mathrm{W/(m^2 \cdot K)}$ natural convection heat transfer coefficient. (**b**) The inner conductor of the coupler is set to a $0.1\ \mathrm{W/(m^2 \cdot K)}$ natural convection heat transfer coefficient and the outer conductor at air end is set to a $5\ \mathrm{W/(m^2 \cdot K)}$ forced convection heat transfer coefficient

Copper plating was applied to the inner surface of the outer conductor to minimize the RF power loss associated with stainless steel surfaces. The selection of an appropriate thickness of high-quality copper, characterized by its residual resistivity ratio (RRR), is critical for reducing RF power loss. However, it is worth noting that an increase in thermal conductivity may lead to a corresponding increase in static heat leakage. Huang et al. systematically investigated the effects of the copper-plating thickness and the RRR value of copper on the heat leakage of couplers [16]. Their findings indicate that a copper-plating thickness ranging from 3δ to 5δ can sufficiently reduce power losses, whereas a copper layer with a thickness of 3δ and an RRR value between 10 and 30 can effectively reduce the total heat load, where δ is the skin depth ($\delta_{81.25\,\mathrm{MHz}} \approx 8.5\,\mu\mathrm{m}$). Therefore, to further reduce the total heat leakage, the outer conductor of the QWR coupler is made of 1 mm thick stainless steel and its inner surface is plated with a 30-micron-thick copper layer with an RRR of 10.

The 5 K helium gas cooling method is more effective in reducing heat leakage from the coupler than the thermal anchor cooling scheme [30]. Figure 9 illustrates the design used for cooling the outer conductor on the vacuum side of the QWR coupler. The design utilizes a double-walled structure with an internal helical flow channel, and the helium gas inlet is located near the flange connecting the cavities. According to the design of the cryomodule of the QWR superconducting cavity, the interface between the cryomodule and coupler has a diameter of 4 mm; thus, the diameter of the helium pipe was selected to be 4 mm. The variation in the total heat leakage at 2 K in the FPC was evaluated for a continuous-wave power of 6 kW in the traveling-wave mode at a helium inlet temperature of 5 K and different helium mass flow rates. Figure 10 shows the relationship between the mass flow rate of helium gas and the total heat leakage. As shown in Fig. 10, heat leakage is minimized when the mass flow rate of helium gas is chosen to be 50 mg/s. Table 3 lists the total heat leakage with different cooling methods, where the boundary condition for the "without any cooling" term is set to $0.1\,\mathrm{W/(m^2 \cdot K)}$ for the heat transfer coefficient of the inner conductor of the coupler and to $5\,\mathrm{W/(m^2 \cdot K)}$ for the heat transfer coefficient of the outer conductor of the air side of the coupler. The "30 μm RRR 10 copper plating" term corresponds to the addition of a 30 μm thick, RRR 10 copper-plating layer to the "without any cooling" condition. The "50 mg/s 5 K gas helium" term corresponds to the addition of 50 mg/s gas helium to the "30 μm RRR 10 copper plating" condition. The 5-K helium gas cooling method effectively reduces the total heat leakage from the FPC and lowers the risk of thermal breakdown of the superconducting cavity.

Mechanical and thermal analyses of the ceramic window of the 5 K gas-helium-cooled couplers with an optimal copper-plating thickness while transmitting 6 kW of continuous-wave power were performed using COMSOL [27]. Figure 11(a) shows the temperature distribution of the ceramic window, which has a maximum temperature of 305 K and a maximum temperature difference of 5 K for the ceramic window assembly. The maximum thermal stress shown in Fig. 11(b) is 14.3 MPa, which is much lower than the flexural strength of 97.6% alumina (296 MPa). Therefore, the risk of the ceramic window cracking is small.

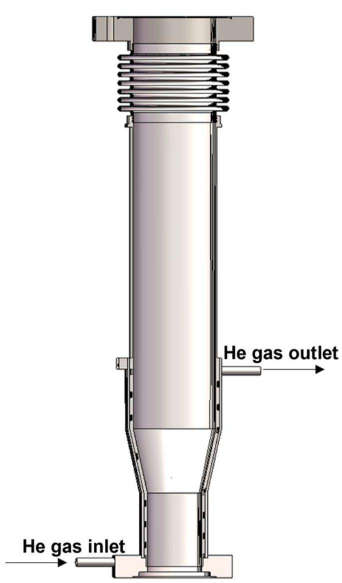

Fig. 9 (Color online) Double-walled structure of the outer conductor for helium gas cooling

4 Multipacting analysis

Multipacting (MP) in the coupler directly affects the normal operation of the coupler. The electrons generated on the inner surface of the coupler absorb the RF power, and

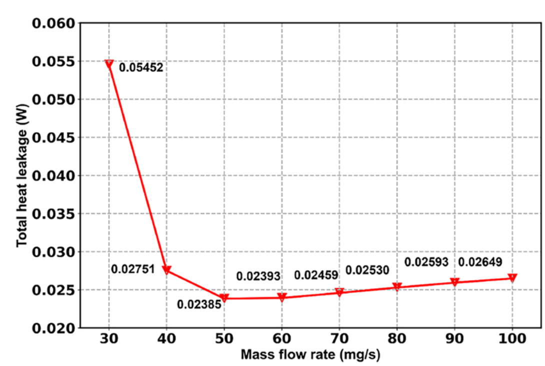

Fig. 10 (Color online) Total heat leakage from the coupler as a function of the mass flow rate of helium

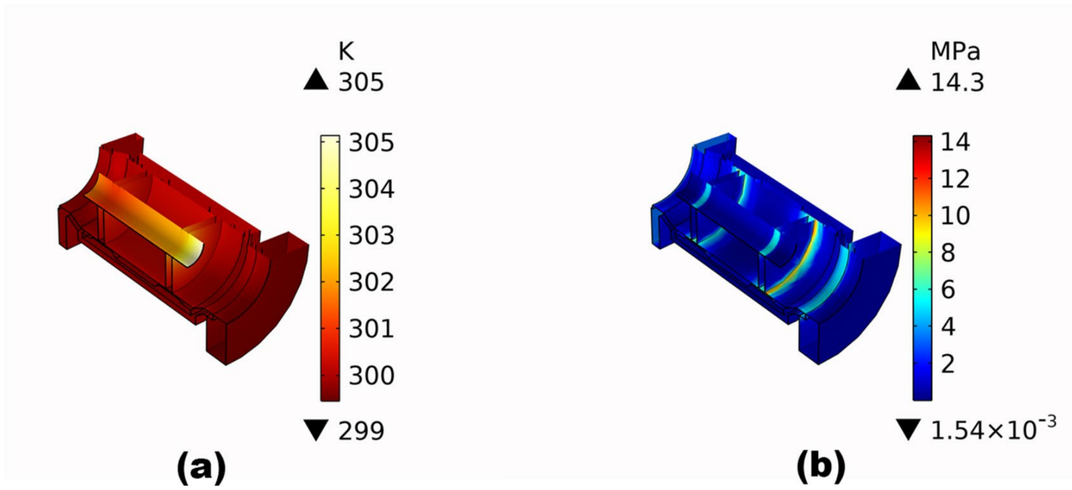

Fig. 11 (Color online) (**a**) Temperature distribution of the ceramic windows assembly. (**b**) Thermal stress distribution of the ceramic windows assembly

Table 3 Total heat leakage at 2 K for a power of 6 kW CW in the traveling-wave mode across various cooling methods

Cooling method	Total heat leakage (W)
Without any cooling	2.7376
30 μm RRR 10 copper plating	2.0291
50 mg/s 5 K gas helium	0.02385

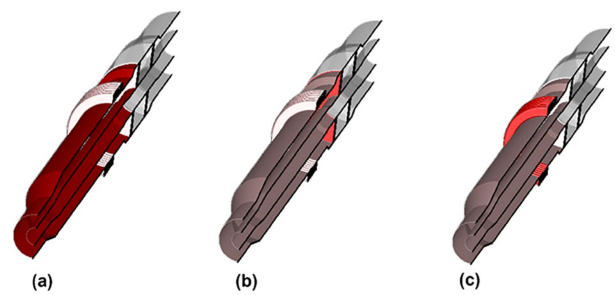

Fig. 12 (Color online) Initial particle area sources. (**a**) Particle source 1: the inner surface of the transmission section. (**b**) Particle source 2: the vacuum side of the ceramic window. (**c**) Particle source 3: the bellows

the charged particles with relatively high energy constantly impinge upon the outer wall of the coupler and the ceramic window. Severe MP leads to the degradation of the coupler performance and even destroys the vacuum sealing function of the coupler [31]. MP analysis is used to identify areas where MP occurs, and appropriate and effective methods are used to suppress it. In our study, we employed the tracking solver in CST Particle Studio [24] for MP simulations. To quantify the occurrence of MP more intuitively, a particle number growth factor is used to determine the likelihood of MP. The corresponding exponential growth factor β is calculated by fitting the curve of the number of emitted particles versus time to an exponential function, that is, $N = N_0 e^{\beta \frac{\Delta T}{T}}$, where β denotes the particle number growth factor, N_0 denotes the initial number of particles, N is the number of electrons after a time interval ΔT, and T is the RF period. A positive β indicates the occurrence of MP, and a negative β indicates that there is no MP. The secondary electron multiplication coefficients of copper, alumina, and titanium nitride (TiN) can be found in Ref. [32–34].

Figure 12 shows the three initial particle sources setup for the MP simulation: the vacuum side of the ceramic window, the bellows, and the inner surface of the coupler transmission section. The inner surfaces of the outer and inner conductors of the coupler are composed of copper, whereas the ceramic window is composed of alumina. The initial electron counts in these three regions were 3408, 3150, and 3986, respectively. Figure 13 shows the particle number growth factor β for the emission of the initial electrons from the three particle area sources at different power levels from 1 kW to 9 kW in steps of 1 kW, where the phase of the source electrons varies from 0° to 300° in steps of 60° for each power level. As shown in Fig. 13, the simulation results indicate that MP may occur at all scanning power ranges. This may be due to the partial bellows in the outer conductor of the coupler, which are characterized by a very small gap between the waves and slots, resulting in a higher field strength and, therefore, an increase in the probability of the occurrence of MP. The coupler must employ an appropriate MP suppression

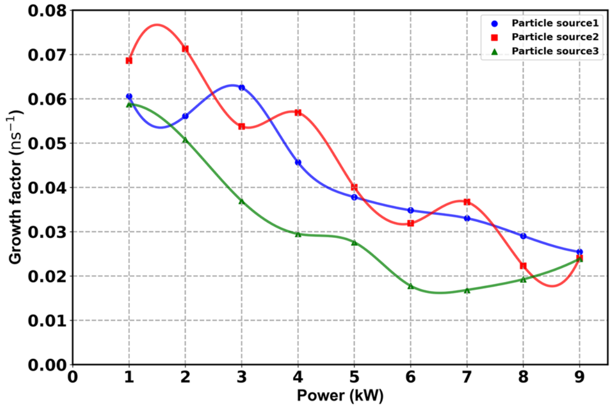

Fig. 13 (Color online) Relationship between different input powers and growth factors corresponding to particle area sources

method to mitigate or eliminate MP under the operating power.

MP simulation results clearly demonstrate the need for MP suppression methods. There are several methods for suppressing MP in couplers. Common methods include coating the inner and outer conductors, as well as the vacuum side of the ceramic window, with a thin layer (a few nanometers thick) of low secondary electron-yield materials such as titanium or TiN. In addition, applying a DC bias voltage to the coupler can break the resonance that occurs during MP. Therefore, the QWR coupler employs a 10-nm TiN coating on the vacuum side of the ceramic window and applies a positive DC bias to the inner conductor to suppress the occurrence of MP in the coupler [35]. The MP suppression effect of TiN and various biasing DC voltages ranging from 500 V to 1000 V were investigated. The QWR coupler is designed to operate at a power of 6 kW; however, to ensure the stability of the coupler's performance and minimize the uncertainty factor in the clean assembly of the coupler, a suitable bias voltage is selected to suppress the occurrence of MPs for power ranges from 1 kW to 9 kW and ensure that the coupler can be adapted to variable operating conditions. Figure 14 shows plots of the growth factors in the input power range from 1 kW to 9 kW for different DC bias voltages, with the boundary conditions set for a TiN material with a low secondary electron yield at the vacuum side of the ceramic window. Figure 14(a) shows that a bias voltage of 600 V can suppress the occurrence of MP with an input power in the range of 1–9 kW for particle source 1. As shown in Fig. 14(b), DC bias voltages of 600 V and above can suppress the MP-generated power range of 1 kW to 9 kW for particle source 2. Figure 14(c) illustrates the effect of different DC bias voltages on the suppression of MP occurrence in the coupler bellows. A DC bias voltage of at least 800 V is required to suppress the MP generation of particle source 3 in the power range of 1 kW to 9 kW. According to the simulation results shown in Fig. 14, we finally chose a DC bias voltage of 800 V to suppress all MP occurrences in the coupler, with an input power in the range of 1 kW to 9 kW.

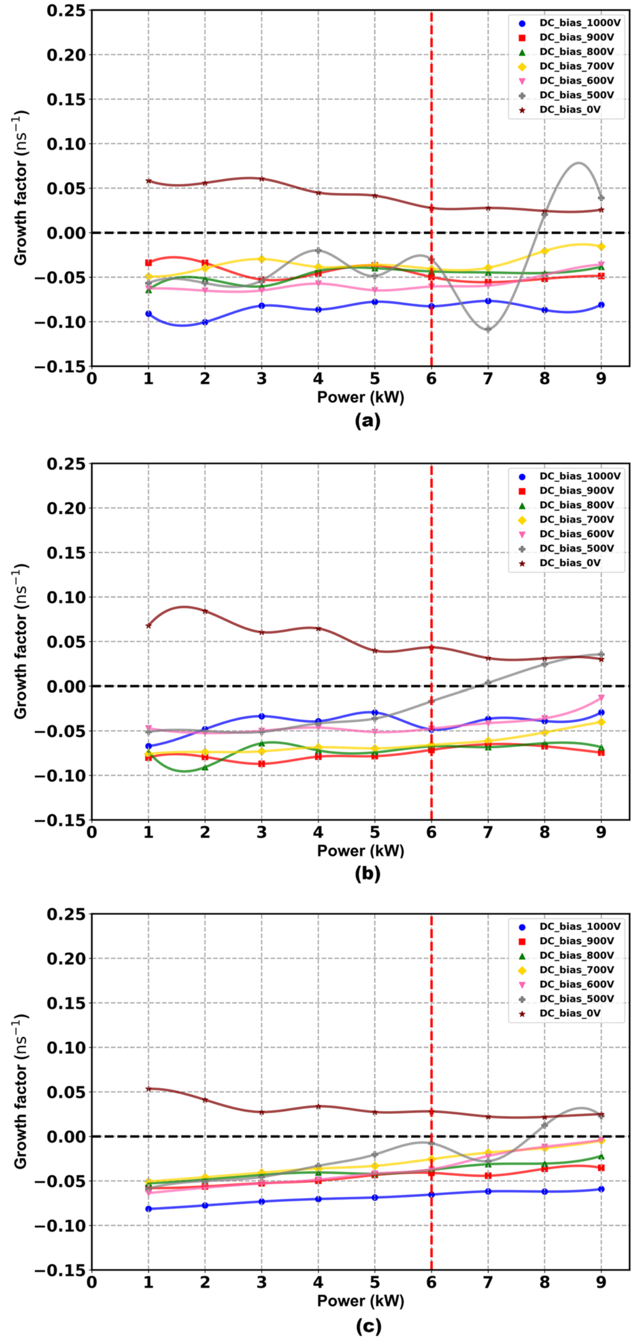

Fig. 14 (Color online) Growth factors corresponding to various particle area sources versus different DC bias voltage. (**a**) Particle source 1. (**b**) Particle source 2. (**c**) Particle source 3

5 Mechanical design and fabrication

Once the physical designs were completed, the mechanical designs of the QWR couplers were initiated. Each coupler contains three main subcomponents: a coaxial transmission section on the vacuum side of the coupler, a dual-disk warm-window assembly, and a T-box. These subassemblies are made from a variety of materials such as 316 L and 304 stainless steel, oxygen-free high-thermal-conductivity copper (OFHC), aluminum alloys, and 97.6% alumina ceramic.

The outer conductor of the vacuum section is made of 304 stainless steel with a wall thickness of 1 mm, and the bellows to which it is connected are also made of 304 stainless steel with a thickness of 0.25 mm. To minimize the total heat leakage, they are plated on the inner surface with 30 micron RRR 10 copper. Considering the high permeability of 304 stainless steel, the flange of the coupler outer conductor connecting the superconducting cavity is made of 316 L stainless steel with low permeability. The magnetic shielding layer inside the helium jacket of the QWR superconducting cavity and the 316 L stainless steel flange of the coupler connecting the superconducting cavity work together to reduce the residual magnetic field inside the superconducting cavity to less than 15 mG, which meets the requirements of the IMP for the residual magnetic field of the superconducting cavity. The antenna is hollow and can be cooled by natural air convection to mitigate temperature increases in the inner conductor. The QWR coupler utilizes a dual-disk warm-ceramic-window assembly, and the copper ring is made of OFHC. The coupler incorporates several monitoring ports, such as vacuum and ARC ports, to monitor the vacuum variations and record the RF breakdown counts. The body of the T-box is made of 6061 aluminum alloy, and the capacitor of the T-box is made of polyvinyl film to prevent a high DC bias voltage from damaging the power source system. To achieve adjustability, the QWR coupler, following the design used in Argonne Laboratory [20], employs an adjustable coupling method using an outer conductor bellows. Adjusting the lengths of the three bolts changes the coupling coefficient of the coupler and ensures the eccentricity of the inner and outer conductors.

A thorough mechanical analysis of a dual-disk warm-ceramic-window assembly is imperative for evaluating its performance under various operating conditions, such as transportation, assembly, operation, and testing, which could potentially result in ceramic window rupture or bending of the coupler inner conductor [36]. Mechanical analysis of the coupler was performed using COMSOL Multiphysics [27]. A mechanical model of the coupler ceramic window components and internal conductors is shown in Fig. 15. The boundary conditions were that cryomodule sealing flange and the air-end inner conductor were fixed. The

Table 4 Results of mechanical analysis of ceramic windows and the inner conductor

Direction	Deformation (μm)	Stress (MPa)
Y-axis (−5×gravity)	0.691 (MAX)	1.76 (MAX)
Z-axis (5×gravity)	390 (MAX)	53.9 (MAX)

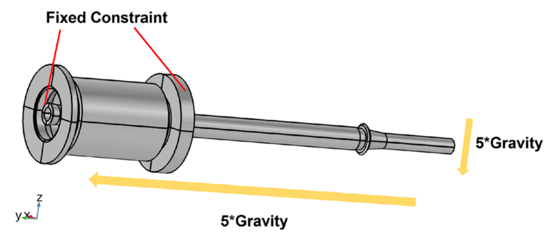

Fig. 15 (Color online) Schematic of the mechanical analysis of the inner conductor and the ceramic windows of the coupler

first model frequency and its degenerate mode frequency were 55.9343 Hz and 55.9371 Hz, respectively. The second model frequency and its degenerate mode frequency were 409.5572 Hz and 409.5578 Hz, respectively. The simulation results show that the model frequencies of the ceramic window assembly and inner conductor of the coupler are well above 50 Hz, which is sufficient to mitigate the resonance of the QWR coupler with external equipment. An axial and lateral load of five times gravity was applied to the ceramic window assembly and inner conductor of the coupler with the same simulation boundary settings. Five times the gravity acting on the inner conductor from the coupling port to the T-box, because the coupler is assembled in a vertically downward direction, and five times the gravity acting on the inner conductor along the Z-axis are considered as the external force to which the coupler may be subjected during transportation or testing. Table 4 lists the deformation and stresses used for the mechanical analysis of the ceramic window assembly and coupler inner conductor. The maximum deformation in the z-direction was 390 μm, which did not significantly affect the coupler performance. The yield strengths of OFHC (σ_{yield} = 69 MPa) and alumina (97.6%, thickness = 6 mm, σ_{yield} = 296 MPa) exceed the maximum stress of the simulation results, as indicated in Table 4. Therefore, the couplers are less prone to ceramic window breakage and large deformations of the inner conductor during transportation, testing, and operation.

Figure 16 shows the detailed manufacturing process of the QWR coupler. The main processing techniques used in the production of QWR couplers include vacuum brazing, electron beam welding (EBW), and tungsten injection gas (TIG) welding. The air-side stainless steel was brazed using TIG welding. The ceramic windows and copper ring were brazed in a vacuum furnace at 800 °C with a silver copper brazing

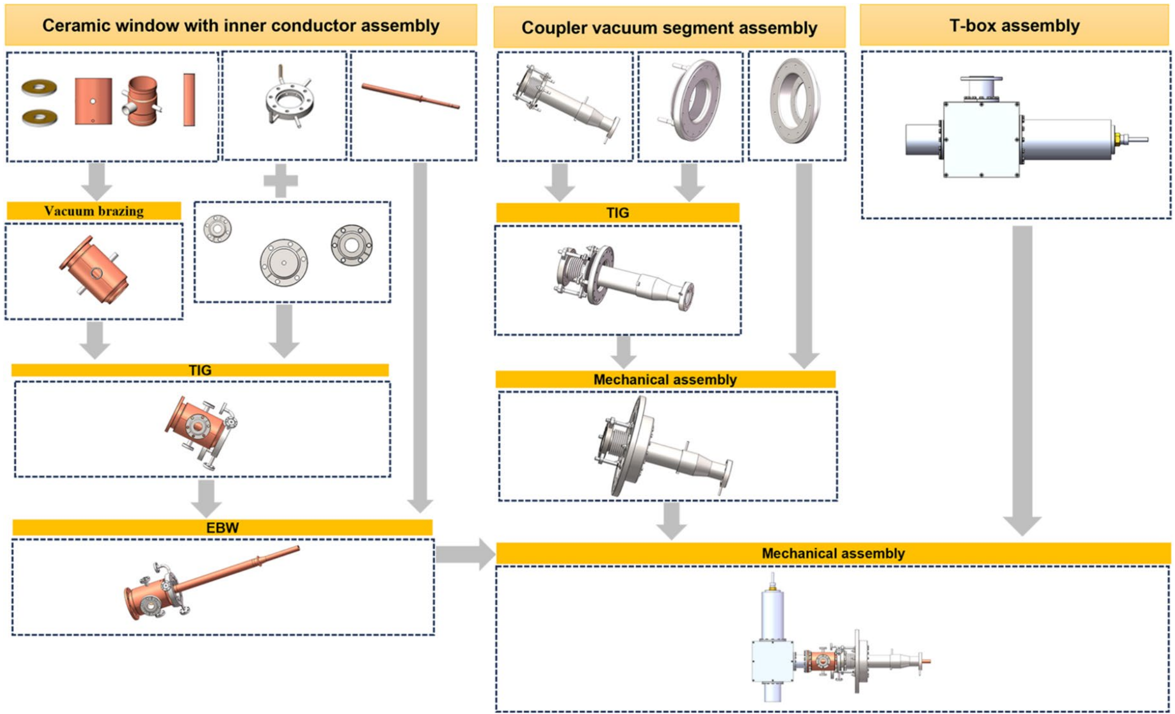

Fig. 16 (Color online) Flowchart of the manufacturing process for the QWR coupler

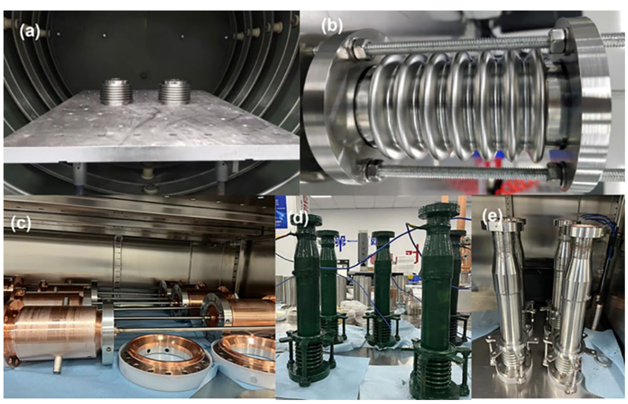

Fig. 17 (Color online) Copper-plating process test for the bellows and QWR coupler subcomponents during the fabrication. (**a**) Vacuum heat treatment of the bellows after copper plating of the inner surface. (**b**) Continuous drawing test (tensile state) of bellows after copper plating the inner surface. (**c**) Ceramic window assembly awaiting processing. (**d**) Copper plating of the coupler's outer conductor's inner surface before performing protective glue treatment. (**e**) Copper-plated coupler's outer conductor storage

material. The inner conductor of the vacuum side and the dual-disk warm-window assembly were welded using EBW to ensure the cleanliness of the vacuum side. Once the parts were machined, they were assembled mechanically. The coating process for the coupler production consists of copper plating and TiN coating with a 10 -nm TiN layer on the vacuum side of the ceramic window coated by magnetron sputtering [37, 38]. Copper plating of the inner surface of the bellows is crucial for the copper-plating process. Three methods were used to test the adhesion of the copper layer on the inner surface of the bellows: vacuum annealing, continuous drawing, and liquid nitrogen thermal shock. Figure 17(a) and (b) shows the copper-plated bellows subjected to vacuum annealing and continuous drawing testing. After the above three tests, there were no obvious wrinkles, peeling, blistering, or delamination on the inner surface of the bellows, indicating that the copper-plating process met the requirements. Figure 17(c), (d), and (e) shows the ceramic window assembly to be machined, the coupler outer conductor to be copper-plated, and the coupler outer conductor

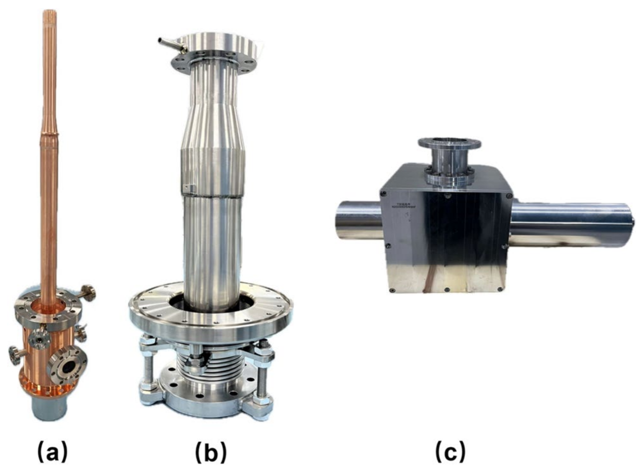

Fig. 18 (Color online) Three main assemblies for the QWR coupler. (**a**) Dual-disk warm-ceramic-window assembly and inner conductor. (**b**) Coaxial transmission section of the vacuum side. (**c**) T-box

after machining. Several critical manufacturing processes for QWR couplers were validated to ensure their repeatability and reproducibility. Figure 18 illustrates the three main assemblies of the QWR coupler. These components were machined. The T-box, outer conductor of the coupler, and ceramic window can be mechanically assembled and prepared for high-power conditioning.

6 Performance verification

The coupler performance was evaluated by analyzing the RF conditioning phenomena. Before installing the cryomodules, each QWR coupler was subjected to high-power RF conditioning at room temperature to a stabilized power level of 9 kW. This testing process can eliminate the surface-adsorbed gases and MP barriers of the coupler and incinerate microscopic surface impurities. This process evaluates the robustness of the coupler [39].

Before high-power conditioning, the coupler underwent a comprehensive cleaning process in which each assembly of the coupler was cleaned in an ultrasonic bath for 25 min. The assemblies were dehydrated using anhydrous ethanol and dried using filtered high-purity nitrogen. The cleanliness of the assemblies was evaluated using a particle counter. Following the assembly, vacuum leak testing must be performed, and the helium vacuum leak rate must be less than 1.0×10^{-8} Pa · L/s. The assembled coupler was positioned on the test bench for in situ baking at a temperature of 150 °C for 72 h. This procedure effectively removes moisture from inside the coupler, thereby minimizing the conditioning time [40].

A high-power conditioning system consists of three main subsystems: a microwave power source and transmission system, a test bench, and a low-level control and protection system [41]. The microwave power source and transmission system primarily consist of a solid-state power source capable of delivering an output power of up to 10 kW. The high-power conditioning mode can be modified by replacing the terminal equipment of the downstream coupler. The test bench comprises a coupler support bracket and a test-connecting cavity, facilitating optimal electrical contact and high transmission efficiency between the two sets of couplers. The low-level control and protection system monitors parameters such as the forward power, reflected power, temperature, vacuum, and ARC. If any of these signals exceed predefined thresholds, the power source is temporarily deactivated to protect the coupler. The interlocking system is activated when the vacuum pressure exceeds 5.0×10^{-5} Pa, and the power source is reactivated once the vacuum pressure falls below 1.0×10^{-5} Pa

Figure 19 shows the schematic of a high-power conditioning system. The forward and reflected powers were measured

Fig. 19 (Color online) Layout schematic of the high-power conditioning of the QWR coupler

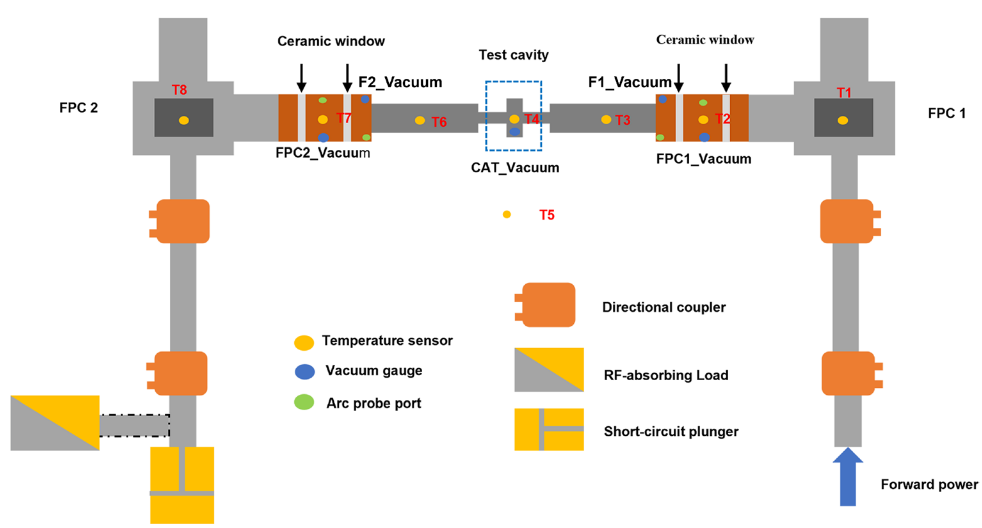

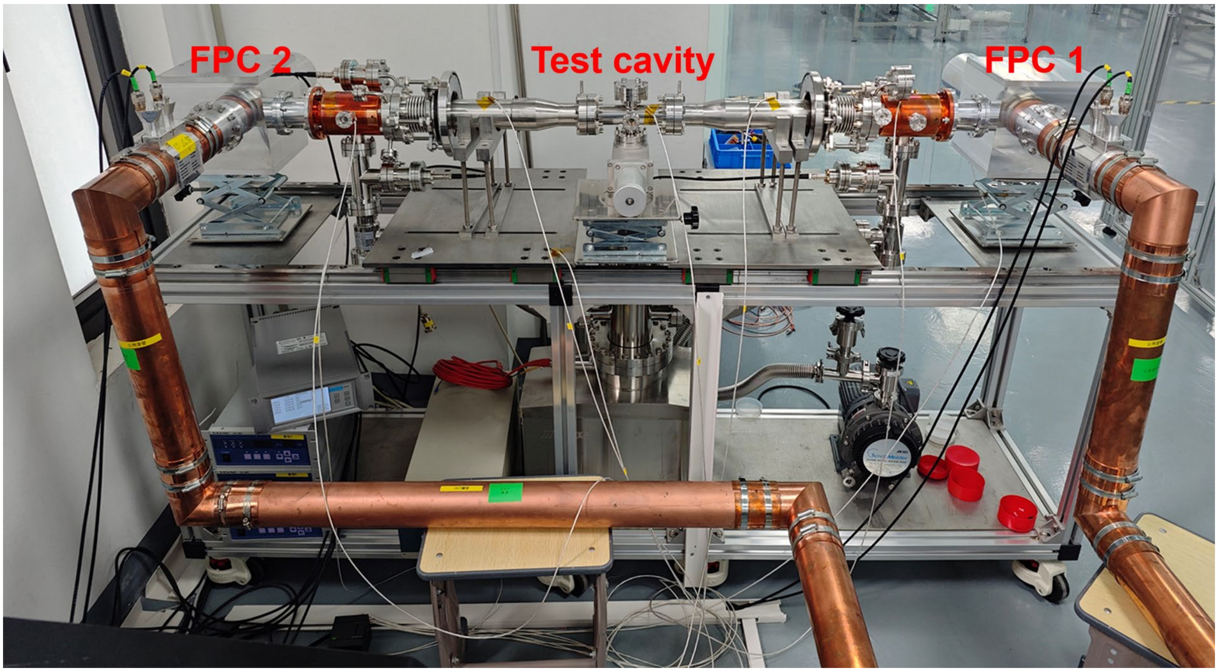

Fig. 20 (Color online) Test bench setup of the power couplers and test cavity

using a directional coupler. The electronic activity of the coupler was measured by monitoring the vacuum changes in the coupler. Seven temperature probes were used to measure the temperature distribution across the couplers. These probes were affixed to specific locations: the inner box of the T-box of FPC 1 (T1), dual-disk warm-window assembly of FPC 1 (T2), outer conductor of the transmission section of FPC 1 (T3), outer conductor of the test cavity (T4), outer conductor of the transmission section of FPC 2 (T6), dual-disk warm-window assembly of FPC 2 (T7), and inner box of FPC 2 (T8). Temperature probe T5 was used to monitor the ambient temperature. Four ARC detectors were installed in the ceramic window sandwich and vacuum sides of FPC 1 and FPC 2.

Figure 20 shows the test bench setup, which consists of two power couplers and a test cavity. The QWR coupler was evaluated during high-power conditioning using a hybrid approach involving the traveling and standing wave modes for QWR coupler fabrication and performance. High-power conditioning specifications were devised for QWR couplers. First, traveling-wave conditioning was performed in the CW mode, and the power

Fig. 21 (Color online) Results of the high-power conditioning test of FPC 1 and FPC 2 in the continuous-wave 9 kW standing wave mode. No DC bias voltage is applied

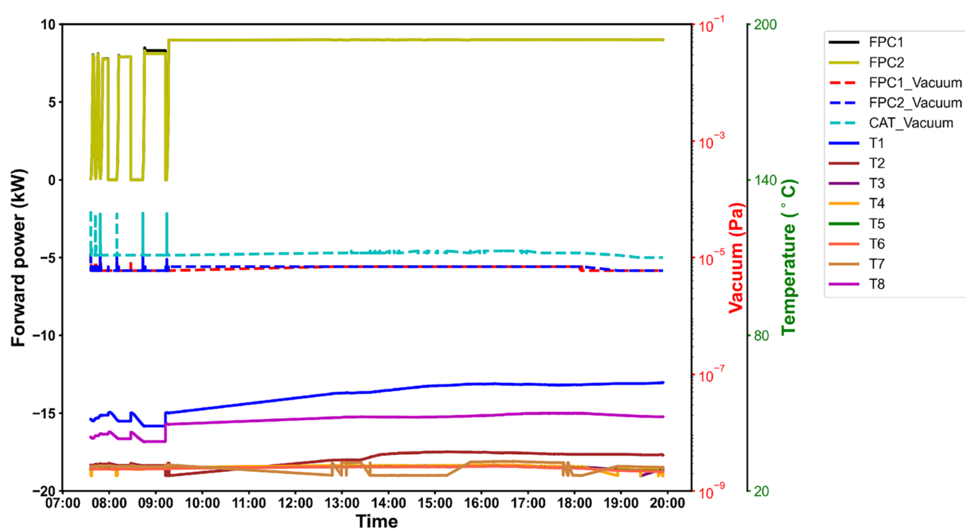

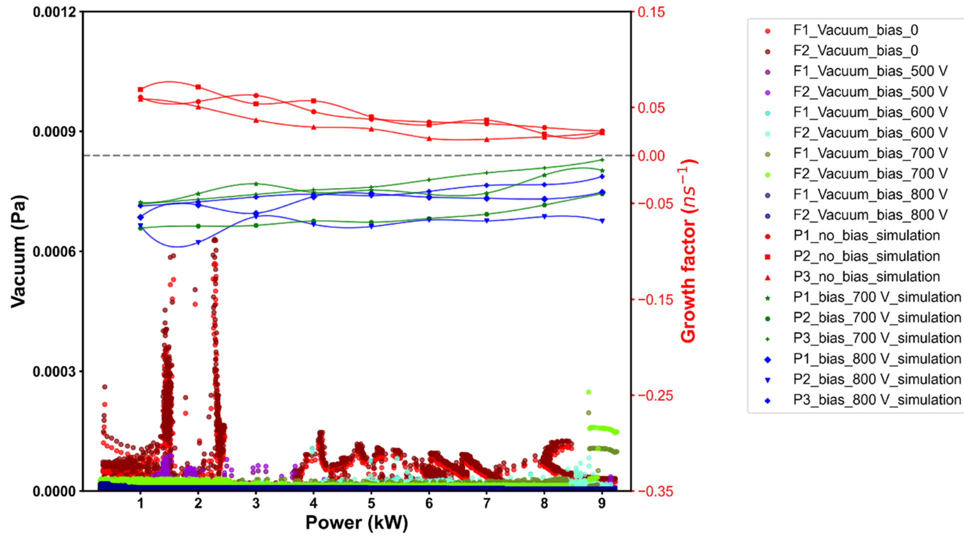

Fig. 22 (Color online) MP test results with different DC bias voltage conditions

was gradually increased from 1 kW to 9 kW and then maintained at 9 kW for 10 h. Thus, the main purpose of traveling-wave conditioning is to pre-degas the couplers. Standing wave conditioning was then performed with an adjustable short-circuit plunger in place of the terminating load, and the position of the short-circuit end was adjusted in steps of 1/16 wavelength (3689 mm) for a total length of 1/2 wavelength to ensure that all the RF surfaces of the coupler were conditioned. In the standing wave mode, the incident power was adjusted to a CW power of 9 kW for the standing wave conditioning of the coupler. As shown in Fig. 21, after an RF power of 9 kW is applied for 2 h, these two couplers can reach a stable power level of 9 kW, the vacuum state of both couplers is stable, and the interlocking protection of the system is not triggered. However, the temperature of T1 increased slightly and then stabilized relative to that T8, because the T1 temperature probe was attached to the copper piece that connected the inner conductor to the inner box of the T-box, whereas the T8 temperature probe was mounted on the inner wall of the inner box away from the copper plate. During standing wave conditioning, the temperature of the inner conductor increased, resulting in an increase in T1. In future experiments, the location of the T1 probe will be changed to the inner wall of the inner box. The total conditioning time for these two prototype couplers was 22 h, with 10 h of traveling-wave conditioning and 12 h of standing wave conditioning, during which no ARC events occurred.

MP is verified using traveling-wave conditioning. MP causes the vacuum of the couplers to deteriorate. Therefore, we characterized the level of MP occurrence in terms of the vacuum of the coupler. The vacuum variations in the coupler at different power levels during traveling-wave conditioning were recorded. F1_vacuum and F2_vacuum in Fig. 19 are the MP-verified vacuum measurement ports. Figure 22 shows the vacuum variations in the two couplers for input powers ranging from 1 kW to 9 kW at different DC bias voltages. In the absence of a DC bias voltage, the coupler suffered vacuum deterioration in the input power range of 1 kW to 9 kW. In the range of 1 kW to 3 kW, the vacuum deterioration was severe; the results of this test agree with the simulation results that the growth factor of MP in the absence of a DC bias voltage decreases progressively from 1 kW to 9 kW. Subsequently, we applied DC bias voltages from 500 V to 800 V and observed the vacuum variations in both couplers. As the bias voltage gradually increased, the vacuum of the coupler gradually stabilized at a lower value. However, a bias voltage of 500 V induced new MP barriers at input powers of 1 kW to 3 kW, and a bias voltage of 600 V generated new MP barriers at input powers of 4 kW to 6 kW. A bias voltage of 700 V cannot effectively suppress MP at the input powers of 8 kW to 9 kW, as predicted by the simulation results. Therefore, the bias voltage was set to 800 V. The input power was scanned from 1 kW to 9 kW, the two couplers were subjected to traveling-wave conditioning, and the vacuum of the two couplers was stabilized. A DC bias voltage of 800 V was found to effectively suppress MP occurrence in the input power range from 1 kW to 9 kW.

7 Conclusion

The fundamental power coupler for the development of the QWR at 81.25 MHz used in the HIAF project is a cutting-edge component designed to meet the rigorous requirements of superconducting RF systems. Two prototype couplers with power capacities of 6 kW were designed, fabricated, and subjected to high-power conditioning tests. The coupler utilized a dual-disk warm-window structure to reduce the risk of vacuum leakage in superconducting RF systems. Simultaneously, to minimize the total heat leakage of the coupler, a double-wall structure was applied to the outer conductor of the coupler to allow for helium gas cooling at 5 K. MP in the coupler was suppressed by applying a DC bias voltage and using TiN material. The selection of materials for coupler processing and feasibility verification of the fabrication process were conducted to reduce the production cost of the coupler and make it suitable for mass production. The couplers were subjected to 10 h of 9 kW traveling-wave conditioning and 12 h of 9 kW standing wave conditioning, finally reaching a stabilized 9 kW power level and stable vacuum. An MP barrier was encountered, as predicted by the simulation results. In the input power range of 1 kW to 9 kW, a DC bias voltage of 800 V effectively suppressed MP in the coupler. These MP barriers were eventually cleared by high-power conditioning. These couplers will be mounted on a cryomodule along with a QWR superconducting cavity for future horizontal testing. We plan to focus on the temperature distribution and multipacting behavior during horizontal cryomodule testing.

Author Contributions All authors contributed to the study conception and design. Material preparation, data collection, and analysis were performed by Guo-Chang Liu, Tian-Cai Jiang, Zhong-Heng Xue, Ji-Yu Wang, Ke-An Jin, Meng-Xin Xu, Zhou-Li Zhang, Chun-Long Li, Qi-Tong Huang, Sheng-Xue Zhang, Sheng-Hu Zhang, and Yuan He. The first draft of the manuscript was written by Guo-Chang Liu, and all authors commented on previous versions of the manuscript. All authors read and approved the final manuscript.

Data Availability The data that support the findings of this study are openly available in Science Data Bank at https://cstr.cn/31253.11.sciencedb.j00186.00948 and https://www.doi.org/10.57760/sciencedb.j00186.00948.

Declarations

Conflict of interest The authors declare that they have no conflict of interest.

References

1. Y. Chen, Y.L. Ye, K. Wei, Progress and perspective of the research on exotic structures of unstable nuclei. Nuclear Techniques (in Chinese) **46**(8), 080020 (2023). https://doi.org/10.11889/j.0253-3219.2023.hjs.46.080020
2. X. Zhou, M. Wang, Y.H. Zhang et al., Bρ-defined isochronous mass spectrometry at the storage ring CSRe. Nucl. Sci. Tech. **35**, 213 (2024). https://doi.org/10.1007/s41365-024-01587-y
3. H.Y. Deng, Y.M. Xing, X. Zhou et al., Improved isochronous mass spectrometry with tune measurement. Nucl. Sci. Tech. **35**, 203 (2024). https://doi.org/10.1007/s41365-024-01580-5
4. S.B. Ma, L.N. Sheng, X.H. Zhang et al., Opportunities for production and property research of neutron-rich nuclei around $N = 126$ at HIAF. Nucl. Sci. Tech. **35**, 97 (2024). https://doi.org/10.1007/s41365-024-01454-w
5. X. Zhou, J. Cheng, the HIAF project team, Status of the high-intensity heavy-ion accelerator facility in China. AAPPS Bull. **32**, 35 (2022). https://doi.org/10.1007/s43673-022-00064-1
6. J. Yang, G. Xiao, H. Xu et al., High intensity heavy ion accelerator facility (HIAF) in China. Nucl. Instrum. Methods Phys. Res. Sect. B **317**, 263–265 (2013). https://doi.org/10.1016/j.nimb.2013.08.046
7. J.C. Yang, L.T. Sun, Y.J. Yuan, Status of the HIAF accelerator facility in China. In Proceedings of the 23rd International Conference on Cyclotrons and their Applications, Beijing, China, Dec 2022, paper MOAI01, pp. 1–5. doi: 10.18429/JACoW-CYCLOTRONS2022-MOAI01
8. M. Xu, Y. He, S. Zhang et al., Low beta superconducting cavity system design for HIAF iLinac. Nucl. Eng. Technol. **55**, 2466–2473 (2023). https://doi.org/10.1016/j.net.2023.04.010
9. S. Posen, M. Liepe, Mechanical optimization of superconducting cavities in continuous wave operation. Phys. Rev. ST Accel. Beams **15**, 022002 (2012). https://doi.org/10.1103/PhyRevSTAB.15.022002
10. S. Ghosh, P.N. Patra, B.K. Sahu et al., Method to reduce microphonic in superconducting resonators. Phys. Rev. ST Accel. Beams **10**, 042002 (2007). https://doi.org/10.1103/PhysRevSTAB.10.042002
11. I.E. Campisi, Fundamental power couplers for superconducting cavities. In Proceedings of the 10th Workshop on RF Superconductivity, Tsukuba, Japan, Sept 2001, paper FA005, pp. 132–143. https://jacow.org/srf01/papers/FA005.pdf
12. J. Yoon, C.S. Park, J. Bahng et al., Development of antenna adjustable power coupler for 325 MHz superconducting cavities. Nucl. Instrum. Methods Phys. Res. Sect. A **1010**, 165484 (2021). https://doi.org/10.1016/j.nima.2021.165484
13. M. Fan, H. Liu, A. Li et al., Multipacting study of power couplers for the CSNS DTL. Nucl. Instrum. Methods Phys. Res. Sect. A **953**, 163067 (2020). https://doi.org/10.1016/j.nima.2019.163067
14. I.E. Campisi, State of the art power coupler for superconducting RF cavities. In Proceedings of EPAC 2002, Paris, France, Jun 2002, paper TUXGB002, pp. 144–148. https://jacow.org/e02/papers/TUXGB002.pdf
15. H. Jenhani, T. Garvey, A. Variola, RF conditioning studies of input power couplers for superconducting cavities operating in pulsed mode. Nucl. Instrum. Methods Phys. Res. Sect. A **595**, 549–560 (2008). https://doi.org/10.1016/j.nima.2008.07.111
16. T. Huang, P. Zhang, Q. Ma et al., Development of fundamental power coupler for 166.6 MHz superconducting quarter-wave beta = 1 proof-of-principle cavities. Rev. Sci. Instrum. **91**, 063301 (2020). https://doi.org/10.1063/5.0001540
17. S. Lee, J. Lee, B. Choi et al., Development of the fundamental power coupler for the quarter wave resonator in the rare isotope science project. J. Korean Phys. Soc. **76**, 632–637 (2020). https://doi.org/10.3938/jkps.76.632
18. Y. Gómez-Martínez, F. Vezzu, T. Cabanel et al, Last SPIRAL 2 10kW CW RF coupler design. In Proceedings of LINAC08, Victoria, Canada, Sept-Oct 2008, paper THP076, pp. 969–571. https://jacow.org/LINAC08/papers/THP076.pdf
19. M.V. Lalayan, T.A. Bakhareva, M. Gusarova et al., Input power coupler for NICA injector coaxial quarter wave SC cavity. In Proceedings of the 18th International Conference on RF Superconductivity, Lanzhou, China, Jul 2017, pp. 61–63. https://jacow.org/srf2017/papers/MOPB008.pdf
20. M.P. Kelly, Z.A. Conway, M. Kedzie et al., Compact 4kW variable RF power coupler for FRIB quarter-wave cavities. In Proceedings of LINAC2012, Tel Aviv, Israel, Sept 2012, paper TUPB093, pp. 678–680. https://jacow.org/LINAC2012/papers/TUPB093.pdf

21. S.V. Kutsaev, M.P. Kelly, P.N. Ostroumov, Design of RF power coupler for superconducting cavities. J. Instrum. **7**, P11004 (2012). https://doi.org/10.1088/1748-0221/7/11/P11004
22. K. Ozeki, O. Kamigaito, H. Okuno et al., Crymodule and power coupler for RIKEN superconducting QWR. In Proceedings of LINAC2016, East Lansing, MI, USA, Sept 2016, pp. 598–600
23. W. Xu, J. Fite, D. Holmes et al., Broadband high power rf window design for the BNL electron ion collider. Phys. Rev. Accel. Beams **25**, 061001 (2022). https://doi.org/10.1103/PhysRevAccelBeams.25.061001
24. CST–Computer simulation technology. http://www.cst.com
25. I.A. Aponte, B. Esser, Z.C. Shaw et al., Fundamental study of DC and RF breakdown of atmospheric air. Phys. Plasmas **26**, 123512 (2019). https://doi.org/10.1063/1.5119152
26. Z.Y. Ma, J.F. Chen, Design optimization of 3.9 GHz fundamental power coupler for the SHINE project. Nucl. Sci. Tech. **32**(11), 132 (2021). https://doi.org/10.1007/s41365-021-00959-y
27. COMSOL multiphysics. http://www.comsol.com
28. Index of material properties–Properties of solid materials from cryogenic- to room-temperatures (National Institute of Standards and Technology, USA). https://trc.nist.gov/cryogenics/materials/materialproperties.htm
29. R.A. Matula, Electrical resistivity of copper, gold, palladium, and silver. J. Phys. Chem. Ref. Data **8**, 1147–1298 (1979). https://doi.org/10.1063/1.555614
30. K.X. Gu, F. Bing, W.M. Pan et al., Development of fundamental power coupler for C-ADS superconducting elliptical cavities. Chin. Phys. C **41**, 067001 (2017). https://doi.org/10.1088/1674-1137/41/6/067001
31. F. Shen, X. Wang, W. Cui et al., Statistical computation for multipactors in arbitrary microwave devices. IEEE Trans. Microw. Theory Tech. **71**, 4318–4326 (2023). https://doi.org/10.1109/TMTT.2023.3260957
32. W. Xu, Z. Altinbas, S. Belomestnykh et al., Design, simulations, and conditioning of 500 kW fundamental power coupler for a superconducting rf gun. Phy. Rev. ST. Accel. Beams **15**, 072001 (2012). https://doi.org/10.1103/PhysRevSTAB.15.072001
33. D. Wang, Z. Mao, Z. Ye et al., Ultralow electron emission yield achieved on alumina ceramic surfaces and its application in multipactor suppression. J. Phys. D Appl. Phys. **55**, 455301 (2022). https://doi.org/10.1088/1361-6463/ac86df
34. S. Suharyanto, Y.S. Michizono et al., Secondary electron emission of TiN-coated alumina ceramics. Vacuum **81**, 799–802 (2007). https://doi.org/10.1016/j.vacuum.2005.11.062
35. P.N. Ostroumov, S. Kazakov, D. Morris et al., Suppression of multipacting in high power RF couplers operating with superconducting cavities. Nucl. Instrum. Methods Phys. Res. Sect. A **865**, 77–80 (2017). https://doi.org/10.1016/j.nima.2017.02.081
36. Y. Gómez-Martínez, F. Vezzu, T. Cabanel et al., Last SPIRAL 2 10 kW CW RF coupler design. In Proceedings of LINAC08, Victoria, Canada, Sept-Oct 2008, paper THP076, pp. 969–971. https://jacow.org/LINAC08/papers/THP076.pdf
37. W. Kaabi, A. Brinkmann, G. Keppel et al., Titanium nitride coating as a multipactor suppressor. In Proceedings of IPAC'10, Kyoto, Japan, May 2010, paper WEPEC002, pp. 2887–2889. https://accelconf.web.cern.ch/IPAC10/papers/WEPEC002.pdf
38. Z.Y. Ma, S.H. Zhao, X.M. Liu et al., Manufacturing studies and rf test results of the 1.3 GHz fundamental power coupler prototypes. Phys. Rev. Accel. Beams **25**, 113501 (2022). https://doi.org/10.1103/PhysRevAccelBeams.25.113501
39. Z.Y. Ma, S.J. Zhao, X.M. Liu et al., High RF power tests of the first 1.3 GHz fundamental power coupler prototypes for the SHINE project. Nucl. Sci. Tech. **33**, 10 (2022). https://doi.org/10.1007/s41365-022-00984-5
40. H. Jenhani, Preparation and conditioning of the TTF VUV-FEL power couplers. In Proceedings of the 12th International Workshop on RF Superconductivity, Cornell University, Ithaca, New York, USA, Jul 2005, paper THP48, pp. 574–576. https://jacow.org/SRF2005/papers/THP48.pdf
41. L. Chen, S.H. Zhang, Y.M. Li et al., Room-temperature test system for 162.5 MHz high-power couplers. Nucl. Sci. Tech. **30**, 7 (2019). https://doi.org/10.1007/s41365-018-0531-9